

Back Electron Transfer from TiO₂ Nanoparticles to Fe^{III}(CN)₆³⁻: Origin of Non-Single-Exponential and Particle Size Independent Dynamics

Yu-Xiang Weng, Yong-Qiang Wang, John B. Asbury, Hiren N. Ghosh, and Tianquan Lian*

Department of Chemistry, Emory University, Atlanta, Georgia 30322

Received: July 21, 1999; In Final Form: October 15, 1999

Back-electron-transfer (ET) dynamics in Fe^{II}(CN)₆⁴⁻-sensitized colloidal TiO₂ nanoparticles are studied using ultrafast pump probe spectroscopy. Excitation of the adsorbate-to-nanoparticle charge-transfer band at 400 nm leads to direct injection of electrons from Fe^{II}(CN)₆⁴⁻ to TiO₂. The kinetics of back electron transfer from TiO₂ to the Fe^{III}(CN)₆³⁻ are measured by monitoring the bleach recovery of the charge-transfer band in the 430–600 nm region. The measured back-ET kinetics are non-single-exponential, and a multiexponential fit requires at least four components on the <1 ns time scale. The kinetics are independent of pump power, indicating a geminate recombination process. Recombination kinetics are very similar in two samples of 5 and 11 nm (A-type) particles prepared from dried nanoparticle powder, but they are noticeably different from those in samples of 3 and 9 nm (B-type) nanoparticles prepared directly from colloids without drying. This result indicates that the back-ET kinetics in this system are more influenced by the surface properties of the nanoparticles than their sizes. Two models with different distributions of trapped electrons are used to describe the back-ET kinetics. Model I assumes a homogeneous distribution of electrons on the surface of the entire particle. This model predicts a large particle size dependence and cannot fit the observed kinetics. Model II assumes a more localized distribution of injected electrons and takes account of relaxation from shallow to deep trap states during the recombination process. This model can fit the back-ET kinetics with three fitting parameters. According to this model, the injected electrons are trapped near the adsorbate, which accounts for the size independent back-ET kinetics. This model also predicts that trapped electrons at longer distance and/or larger trap energy recombine slower. A distribution of distance and trap energy as well as relaxation between trap states give rise to multiexponential back-ET kinetics.

Introduction

Interfacial electron transfer (ET) between semiconductor nanoparticles and molecular adsorbates has been a subject of intense research interest in recent years.^{1–3} The understanding of this fundamental process is essential for the application of semiconductor nanomaterials in photography,⁴ solar energy conversion,⁵ photocatalysis,⁶ and nanoscale devices.⁷ Electron-transfer dynamics in various combinations of semiconductor nanoparticles and molecule adsorbates have been investigated. Among them, dye-sensitized TiO₂ nanoparticles and thin films are one of the most studied systems because of their important application in a new type of solar cell.⁸ Most recent studies found that the forward electron injection from the excited state of strongly adsorbed dye to TiO₂ occurs on the ultrafast time scale.^{9–23} For example, for Ru(dcbpy)₂(NCS)₂-sensitized TiO₂ thin film,^{9,12,16–19} an injection time of ca. 50 fs^{9,12} or faster¹⁹ has been reported. A high photon-to-current conversion efficiency requires fast electron injection as well as slow back electron transfer. Many studies of back electron transfer from TiO₂ to adsorbates have also been reported. The reported back-ET kinetics in different dye-sensitized TiO₂ systems range from a few picoseconds to milliseconds, and from single^{14,15,24–26} to multiexponential.^{27–31} Observations of Marcus inverted region kinetics behavior have also been reported.^{25,26,29} However, it is still unclear whether recombination of electrons occurs through

states near the conduction band edge or trap states in the band gap and how the distribution of trap states affects the back-ET kinetics.

In an effort to gain quantitative understanding of back electron transfer from semiconductor nanoparticles to molecular adsorbates, we examined electron-transfer dynamics in Fe^{II}(CN)₆⁴⁻-sensitized TiO₂ nanoparticles in colloidal solution. Unlike many previously studied dye-sensitized TiO₂ systems, Fe(CN)₆⁴⁻ and TiO₂ form a charge-transfer (CT) complex. Excitation of the charge-transfer band promotes an electron from Fe(CN)₆⁴⁻ to TiO₂ instantaneously, which enables the study of the subsequent back-electron-transfer kinetics on the subpicosecond and longer time scale. More importantly, in charge-transfer complexes, relevant parameters for the back-ET process can be experimentally determined from the optical spectra. It has been well established that in a molecular donor-and-acceptor charge-transfer complex, electronic coupling, reorganization energy, and driving force for the back-ET process can be obtained from the optical absorption spectrum.^{32–34} Resonant Raman spectra of the complex reveal the Franck–Condon active modes and can be used to calculate the inner sphere reorganization energy.^{35,36} With knowledge of these parameters, quantitative prediction of back-ET rates becomes possible.^{32–36} This type of quantitative treatment has yet to be adopted for molecular-donor-to-semiconductor-acceptor charge-transfer complexes.

In a previous paper,²⁷ we reported the electron injection and recombination dynamics in Fe^{II}(CN)₆⁴⁻-sensitized TiO₂ nanoparticles in colloidal solution. We found that electron injection

* To whom correspondence should be addressed. E-mail: tlian@emory.edu.

from $\text{Fe}^{\text{II}}(\text{CN})_6^{4-}$ to TiO_2 was instantaneous upon the excitation of the charge-transfer band at 400 nm. This result is consistent with the direct charge-transfer nature of the optical transition. The back-ET kinetics were non-single-exponential on the picosecond to nanosecond time scale according to our results and continued up to the microsecond time scale on the basis of previous results.^{29,30} However, the origin of the nonexponential behavior was not understood. In this paper, we explore the detailed mechanism of the back-electron-transfer process by measuring back-ET kinetics in nanoparticles of different sizes and comparing with calculations based on Marcus ET rate theory and models of trapped electron distribution.

Experimental Section

Laser System. The back-ET kinetics between TiO_2 colloidal nanoparticle and the adsorbed $\text{Fe}^{\text{II}}(\text{CN})_6^{3-}$ were measured with a femtosecond pump–probe spectrometer. The laser system (Clark-MXR CPA-1000 regenerative amplifier, 1 kHz repetition at 800 nm, 100 fs, 1 mJ/pulse) and experimental setup have been described in detail elsewhere.²⁷ Briefly, the 800 nm fundamental output was split into two parts, one part with pulse energy of 300 μJ /pulse was frequency-doubled in a BBO crystal to generate a 400 nm pump beam. About 6 μJ /pulse of the 800 nm beam taken from the other part was focused onto a 2 mm thick sapphire window to generate a white light continuum. We selected different probe wavelengths by a variable interference filter (from Optical Coating Laboratory Inc.) with a 10 nm band-pass. The probe beam was detected by a photodiode with a variable gain (PDA50 from Thorlabs Inc.). The absorbance change was compared between two adjacent laser pulses (pump blocked and unblocked). The typical noise measured in the absorbance change was 0.1–0.2%. We set the relative polarization between pump and probe at the magic angle of 54.7°, and the pump and probe beam sizes at about 500 and 200 μm , respectively. The sample was flowed in a 250 μm thick cell (from Harrick) driven by a peristaltic pump.

Synthesis of TiO_2 Nanoparticles and $\text{TiO}_2/\text{Fe}(\text{CN})_6^{4-}$ Complex. TiO_2 nanoparticles were prepared by controlled hydrolysis of titanium (IV) tetraisopropoxide in water under deaerated conditions and controlled pH.³⁷ A 5 mL aliquot of $\text{Ti}[\text{OCH}(\text{CH}_3)_2]_4$ (Aldrich, 97%) dissolved in isopropyl alcohol (5:95) was added dropwise (1 mL/Min) to 900 mL of doubly distilled water (2 °C) at a given acidity (around pH = 2) adjusted with HNO_3 . After continuous stirring for 12 h or longer, the solution became transparent and TiO_2 nanoparticles were formed. The sizes of the nanoparticles were measured by dynamic light scattering (Coulter Plus4). We found that the size of the nanoparticles depended critically on the amount of HNO_3 added in the solution. By controlling the amount of added HNO_3 , TiO_2 nanoparticles of varying sizes between 3 and 11 nm were synthesized. To obtain a dried powder sample, the solvent was removed by rotary evaporation at <40 °C, and the resulting white powder was dried in a desiccator with KOH to remove HNO_3 . Two kinds of colloidal solutions were prepared. The first one was prepared by redissolving the dried TiO_2 powder into water (referred to as A-type particles), and the other one was prepared from the TiO_2 colloidal solution obtained in the controlled hydrolysis in water without the drying process (referred as B-type particles). The B-type colloidal solutions were continuously stirred for a few days (after the initial reaction) to ensure stable and more uniform size distribution. Two different sizes of A- and B-type nanoparticles were studied. The average sizes were 3 ± 0.4 and 9 ± 1.5 nm for the B-type particles and 5 ± 1.3 and 11 ± 3.0 nm for the A-type particles.

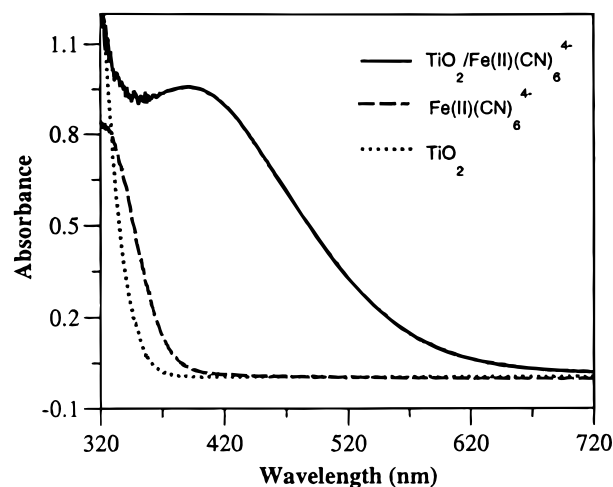


Figure 1. UV/vis spectra of the $\text{Fe}^{\text{II}}(\text{CN})_6^{4-}$ – TiO_2 nanoparticle (3 nm) complex in water at pH = 2 (solid line). Also shown are the spectra for the TiO_2 colloid (dotted line) and $\text{Fe}^{\text{II}}(\text{CN})_6^{4-}$ (dashed line) in water.

The poorer size distribution in A-type particles is attributed to coagulation that occurred during the drying process. The colloidal solution of the A-type TiO_2 nanoparticle was prepared with 10 g/L of TiO_2 . The solution was protected by 10 g/L poly-(vinyl alcohol) (PVA) as a stabilizing agent and adjusted to pH 2 by adding HClO_4 . The colloidal solution was mixed with $\text{K}_4\text{Fe}(\text{CN})_6$ (25 mM), and stirred in the dark under N_2 for >10 h to form the charge-transfer complex. The same procedure was carried out for the sample of B-type particles with smaller concentrations of TiO_2 , PVA, and $\text{K}_4\text{Fe}(\text{CN})_6$ at 1.4 g/L, 1.4 g/L, and 2 mM, respectively.

Results

When TiO_2 nanoparticles were mixed with $\text{Fe}^{\text{II}}(\text{CN})_6^{4-}$ in an acidic aqueous solution, a new absorption band peaked around 420 nm developed, indicating the formation of a CT complex between TiO_2 nanoparticles and $\text{Fe}^{\text{II}}(\text{CN})_6^{4-}$. The complex was thought^{27,38} to form at the surface Ti^{IV} site with a singly CN-bridged structure of C_{4v} symmetry, i.e., $\text{Ti}^{\text{IV}}\text{—NC—Fe}^{\text{II}}(\text{CN})_5$. This notion is supported by both resonant Raman³⁸ and IR²⁷ spectra of the complex. Both show a terminal, radial, and bridging CN stretching band. Shown by the solid line in Figure 1 is a UV/visible spectrum of the charge-transfer complex for 3 nm TiO_2 particles. The peak of the charge-transfer band is centered at about 420 nm. Similar charge-transfer bands were observed for other particle sizes. The dashed and dotted lines indicate the absorption spectra of $\text{Fe}^{\text{II}}(\text{CN})_6^{4-}$ (25 mM) and TiO_2 (10 g/L) in water, respectively.

For the $\text{TiO}_2/\text{Fe}^{\text{II}}(\text{CN})_6$ complex, when excited at 400 nm, near the peak of the CT absorption band, a bleach of the ground-state charge-transfer band was observed in the 430–600 nm region. As can be seen from the UV/vis spectra shown in Figure 1 and from our earlier study,²⁷ 400 nm photons excite almost exclusively the charge-transfer band with negligible direct excitation of $\text{Fe}^{\text{II}}(\text{CN})_6^{4-}$ (25 mM) or TiO_2 . Shown in Figure 2 are typical ground-state bleaching recovery kinetics measured at 450, 500, and 550 nm for the sample of 3 nm B-type TiO_2 particles. These kinetics traces, which were scaled to the value at the peak of the bleach signal for comparison, show no wavelength dependence. To minimize the effect of different pH values in different samples, all solutions were kept at pH = 2. The effect of pH itself was also investigated by comparing the bleach recovery kinetics in samples prepared with the same particle size and preparation procedure except for the pH of

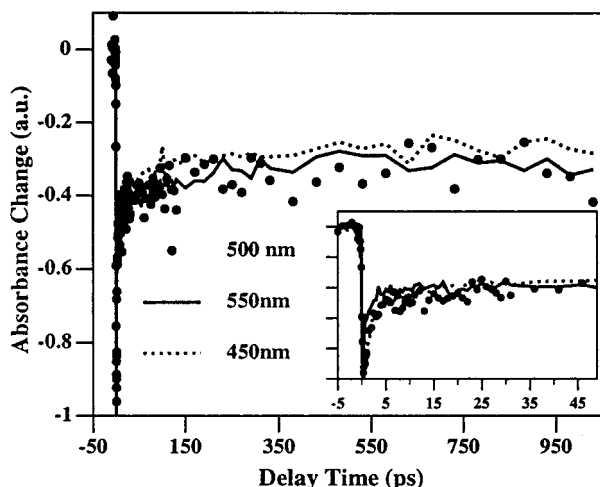


Figure 2. Bleach recovery kinetics in the $\text{Fe}^{\text{II}}(\text{CN})_6^{4-}$ – TiO_2 nanoparticle (3 nm) complex measured at 450, 500, and 550 nm after 400 nm excitation. These kinetics were scaled to have the same signal size at the peak of the bleach. Shown in the inset are the same kinetics on a shorter time scale.

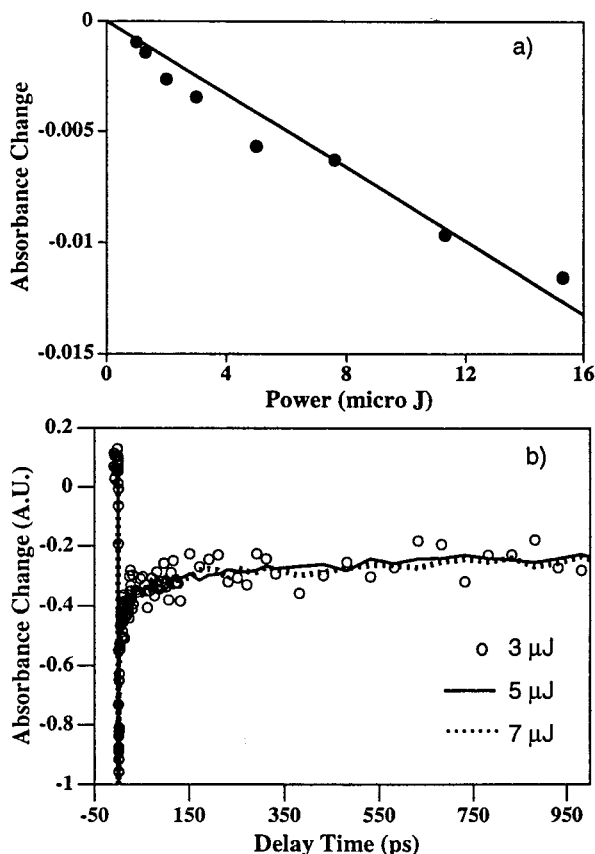


Figure 3. (a) Dependence of the bleach signal on pump power for the $\text{Fe}^{\text{II}}(\text{CN})_6^{4-}$ – TiO_2 nanoparticle (3 nm) complex. (b) Comparison of bleach recovery kinetics at 500 nm for the $\text{Fe}^{\text{II}}(\text{CN})_6^{4-}$ – TiO_2 nanoparticle (3 nm) complex at different pump powers: 3, 5, and 7 μJ . These kinetics were scaled to have the same signal size at the peak of the bleach.

the final solution. In a limited pH range from 2 to 3, in which a stable charge complex could be formed, the bleach recovery kinetics show no pH dependence within the signal-to-noise of the data. To gain more insight into the nature of recombination kinetics, a pump power dependence study was also carried out. Shown in Figure 3a is the power dependence of the bleach signal measured at the peak of the bleach kinetics for sensitized 3 nm B-type particles. As indicated by the straight line, the signal

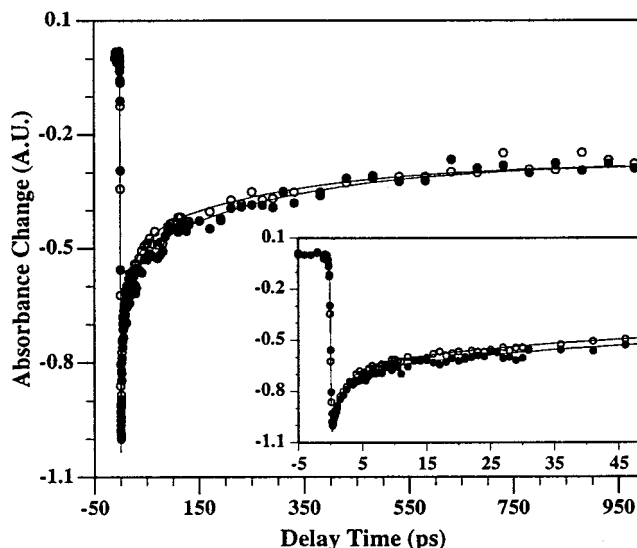


Figure 4. Comparison of the bleach recovery (or back-ET) kinetics of $\text{Fe}^{\text{II}}(\text{CN})_6^{4-}$ -sensitized TiO_2 nanoparticle colloidal solutions prepared from A-type particles with diameters of 5 nm (open circles) and 11 nm (full circles). The solid lines are multiexponential fits to the data with parameters listed in Table 1. Shown in the inset are the same data and fits on a shorter time scale.

TABLE 1: Parameters for the Multiexponential Fits to the Back-ET Kinetics

| sample | A_1 (τ_1 , ps) | A_2 (τ_2 , ps) | A_3 (τ_3 , ps) | A_4 (τ_4 , ns) |
|--------------|------------------------|------------------------|------------------------|------------------------|
| A-type 5 nm | 38% (1.9) | 18% (30) | 19% (300) | 25% (>1) |
| A-type 11 nm | 35% (1.9) | 16% (30) | 23% (300) | 26% (>1) |
| B-type 3 nm | 54% (1.5) | 11% (30) | 8% (300) | 27% (>1) |
| B-type 9 nm | 44% (1.8) | 19% (30) | 9% (300) | 28% (>1) |

size increases linearly with the pump power from 1 to 15 μJ . Shown in Figure 3b are the kinetics of the sample with 3 nm B-type particles at pump powers of 3, 5, and 7 μJ . Within the signal-to-noise of the data, the same kinetics were observed. Similar pump power independent recombination kinetics were found for other TiO_2 colloidal samples.

To investigate the origin of the nonexponential kinetics, we examine the back-ET kinetics in samples of different particle sizes. Shown in Figure 4 are kinetics measured at 500 nm for samples of 5 nm (open circles) and 11 nm (full circles) A-type nanoparticles. Shown in the inset are the same kinetics traces on a shorter time scale. Both kinetics traces were measured under the same experimental condition with 3 μJ of 400 nm excitation and were normalized at the maximum of the bleach for better comparison. These kinetics are identical within the signal-to-noise of the data. The solid lines are fits to the data with four exponential decays. The time constants and pre-exponential factors for the fits are listed in Table 1. At least four exponents are needed to fit the kinetics. The amplitude and time constant of the 30 and 300 ps components are not accurately determined by the fit because of their small amplitudes. The time constant for the >1 ns component cannot be well determined in our fitting since the longest delay time in the data is only 1 ns. To facilitate the comparison of kinetics in different particles, we fixed three time constants (30 ps, 300 ps, and >1 ns) in the fitting and allowed the time constant for the first component and all the amplitudes to vary. As can be seen in Figures 4 and 5, these functions produce satisfactory fits to the data. Size dependence studies of B-type particles were also carried out. Shown in Figure 5 are kinetics measured at 500 nm for samples of 3 nm (open circles) and 9 nm (full circles) B-type nanoparticles. Shown in the inset are similar

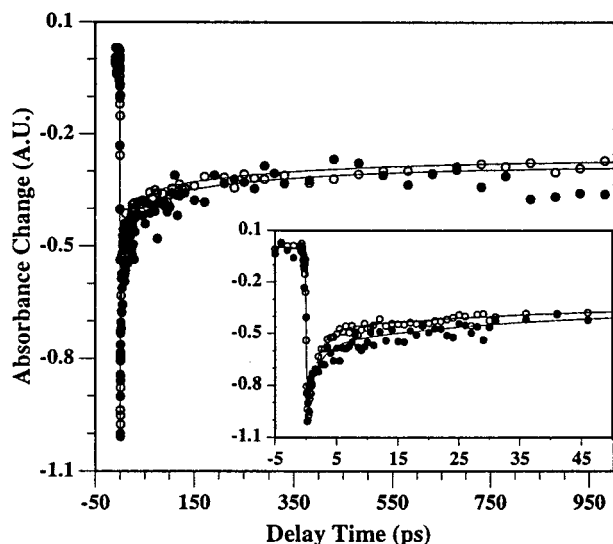


Figure 5. Comparison of the bleach recovery (or back-ET) kinetics of $\text{Fe}^{\text{II}}(\text{CN})_6^{4-}$ -sensitized TiO_2 nanoparticle colloidal solutions prepared from B-type particles with diameters of 3 nm (open circles) and 9 nm (full circles). The solid lines are multiexponential fits to the data with parameters listed in Table 1. Shown in the inset are the same data and fits on a shorter time scale.

kinetics on a shorter time scale. Both kinetics traces were measured under the same experimental condition with 3 μJ of 400 nm excitation and were normalized at the maximum of the bleach for better comparison. The time constants and amplitude for the restricted four-exponential fits to the data are listed in Table 1. Again, the overall kinetics for the two different particle sizes are similar, but there appears to be noticeable difference at the early time. Because of the smaller concentration of nanoparticles used in these B-type samples, the signal-to-noise level of the data are not as good as those in the A-type particles.

Discussion

1. Back-Electron-Transfer Kinetics in TiO_2 - $\text{Fe}^{\text{II}}(\text{CN})_6$ Complex. (a) *Assignment of Bleach Recovery Kinetics.* Excitation of the charge-transfer band at 400 nm promotes electrons from the adsorbate molecules to the nanoparticles. The injected electrons can relax within the nanoparticles and recombine with the oxidized adsorbate. The spectral signatures for the injected electrons, the bleach of the CN stretching bands associated with $\text{Fe}^{\text{II}}(\text{CN})_6^{4-}$, and the absorption due to those of $\text{Fe}^{\text{III}}(\text{CN})_6^{3-}$ have all been identified in the IR region.²⁷ In addition, a bleach of the charge-transfer band in the visible region was also observed. Back electron transfer from the nanoparticle to $\text{Fe}^{\text{III}}(\text{CN})_6^{3-}$ leads to the recovery of the bleach in the CN stretch band in the IR and the charge-transfer band in the visible region. In a previous paper,²⁷ we found that the bleach recovery kinetics measured in the IR were in good agreement with that in the visible. This result demonstrates that for this system, the optical transition in the 430–550 nm region is dominated by absorption of the charge-transfer band and the bleach recovery kinetics can be directly related to back-ET kinetics. In the current study, we only measured recovery kinetics in the visible region for samples of different particle sizes. These measurements yielded data with higher signal-to-noise, allowing for a more critical comparison of back-ET kinetics in particles of different sizes.

On the less than tens of picoseconds time scale, the assignment of the bleach recovery kinetics to back-ET kinetics may be complicated by vibrational relaxation dynamics of hot $\text{Fe}^{\text{II}}(\text{CN})_6^{4-}$ formed after back ET. Ultrafast back ET is expected

to produce vibrationally hot donor and acceptor molecules, as shown recently in intramolecular charge-transfer complexes.^{39–41} The quality of our previous IR data was not adequate to allow for more detailed analysis of the contribution of vibrational relaxation to the bleach recovery dynamics. To ensure that the measured bleach recovery kinetics indeed reflect the back-ET times, we also checked the wavelength dependence of the bleach recovery kinetics at 450, 500, and 550 nm. As shown in Figure 2, within the signal-to-noise of the data, kinetics at these wavelengths are identical. This result indicates that at these wavelengths the contribution of vibrational cooling to the measured kinetics is negligible. Similar wavelength independent kinetics were also observed for three other samples with different particle sizes. In the rest of this paper, only the kinetics at 500 nm are compared.

(b) *Multiexponential ET Kinetics.* As shown in Figures 4 and 5, the measured bleach recovery kinetics at 500 nm can be well fitted typically by four-exponential decays. The fitting results are summarized in Table 1. The typical kinetics contain 1–2 ps, ~30 ps, ~300 ps, and > 1 ns components. The time constant for the > 1 ns component is not well determined in our data. In fact, back ET of $\text{Fe}^{\text{II}}(\text{CN})_6^{4-}$ -sensitized TiO_2 in solution has been studied previously in the nanosecond to microsecond^{29,30} time scale. In an earlier experiment with 20 ns time resolution,³⁰ back ET was measured by monitoring the bleach recovery at 480 nm after 530 nm excitation. Back ET was found to be complete in 10 μs , with a half-life of 3 μs . More recently, in a similar measurement with 2 ns resolution,²⁹ back-ET time was found to be well represented by two components. The fast component, with about 50% of the total amplitude, occurred with a time constant of 270 ns, and the slow nonexponential component appeared to be similar to that observed in the earlier measurement.³⁰ Combining all these results together presents back ET from TiO_2 to $\text{Fe}^{\text{III}}(\text{CN})_6^{3-}$ as a highly nonexponential process. It contains at least five different time constants, ranging from 1 to 2 ps to 3 μs .

(c) *Pump Power Dependence.* To gain some insight into the nature of the recombination kinetics, a pump power dependence study was performed. As shown in Figure 3a, the size of the initial bleach signal is linearly dependent on the pump power, indicating that the excitation step is a single photon event. The recombination kinetics at three different pump powers, 3, 5, and 7 μJ , are identical after scaling the initial bleach to the same value, as shown in Figure 3b. This result suggests that at the pump power level used in the experiment, the recombination process is mostly geminate; i.e., the injected electrons recombine with the adsorbate molecules from which they originate. If the recombination was not geminate, the recombination rate would be dependent on the concentration of the injected electrons, which depends on the pump power. This conclusion is valid when the excitation level is high enough that the probability of creating more than one electron per particle is not negligible. The exact amount of $\text{Fe}^{\text{II}}(\text{CN})_6^{4-}$ that adsorbed on the surface was not accurately determined. On the basis of the IR absorbance change in the CN stretching mode for free $\text{Fe}^{\text{II}}(\text{CN})_6^{4-}$ upon addition of TiO_2 nanoparticles, we estimated that ca. 40% of the molecules were adsorbed on the surface of the 5 nm particles. This corresponds to a surface coverage of 150 molecules per TiO_2 particle. At 3 μJ pumping power, a bleach of 2% was observed, which amounts to an average of 3 injected electrons per particle. Assuming that the number of molecules on the surface of the 3 nm particles can be estimated from that of the 5 nm particles by simply scaling the surface area, we estimated a coverage of 55 molecules per nanoparticle. With

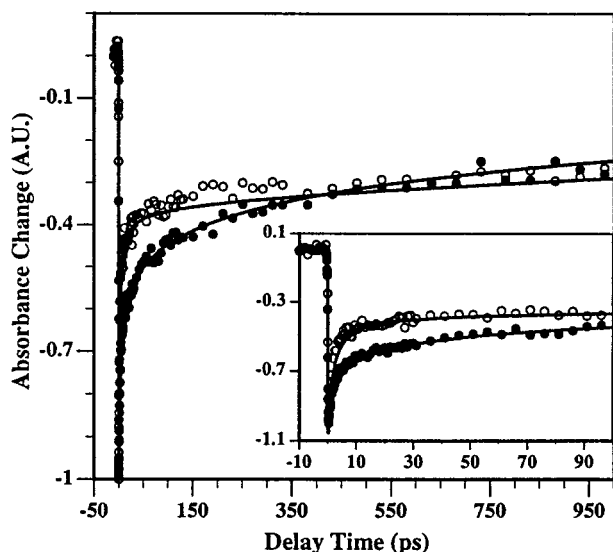


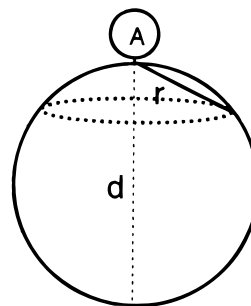
Figure 6. Comparison of the bleach recovery (or back-ET) kinetics of Fe^{II}(CN)₆⁴⁻-sensitized TiO₂ nanoparticle colloidal solutions prepared from 3 nm B-type particles (open circles) and 5 nm A-type particles (full circles). The solid lines are fits to the data according to eq 6 (see the main text) with parameters listed in Table 2 for $\Delta G_0 = -0.94$ V. Shown in the inset are the same data and fits on a shorter time scale.

an observed $\sim 2\%$ bleach, an average of ca. 1.1 electrons was injected per particle in the 3 nm particles at 3 μ J pump power. The average number of injected electrons is bigger for bigger particles and at higher excitation powers. The observation of geminate recombination kinetics, as revealed by the lack of pump power dependence, suggests that the injected electrons are localized near the adsorbate.

(d) Size Dependence. In addition to the non-single-exponential characteristic, the recombination kinetics show very little dependence on the particle size. The kinetics in the 5 and 11 nm A-type particles, shown in Figure 4, are indistinguishable within the S/N ratio of the experiment. Slight differences exist between the kinetics for the 3 and 9 nm B-type particles, as shown in Figure 5. The observed kinetics in all samples show multiexponential behavior. A comparison of the kinetics for the B-type 3 nm particles and A-type 5 nm particles is shown in Figure 6. The difference between these kinetics are bigger than those between the different sized A-type or B-type particles, shown in Figures 4 and 5. The A- and B-type particles were prepared with slightly different procedures. The drying process involved in the preparation of A-type particles removed solvent as well as excess ions and ligands from the nanoparticles. Although the final solution was adjusted to the same pH for both samples, the composition of the surface and interface species may be quite different. The observed difference between the 5 nm A-type particle and the 3 nm B-type particles suggests that different preparation chemistry plays a more important role in the back-ET kinetics than the size of the particles for TiO₂ nanoparticles. The importance of surface chemistry in the back-ET process was also noted previously by Martini et al.²⁵ in their study of the effect of H₂O on the back-ET dynamics in 9-anthracenecarboxylic acid-sensitized TiO₂ nanoparticle in ethanol.

2. Modeling of the Nonexponential Back-ET Kinetics. To obtain more insight into the observed non-single-exponential and nearly size independent kinetics, more quantitative analysis of the kinetics is needed. Non-single-exponential back electron transfer from semiconductor to adsorbates has been observed in both TiO₂^{28–30} and SnO₂^{31,42} colloids and thin films.

SCHEME 1



Qualitatively, nonexponential kinetics indicate a distribution of electron-transfer rates. According to Marcus theory for non-adiabatic electron transfer, the ET rate depends on the driving force for the reaction, the electronic coupling matrix element and the reorganization energy. A distribution of each of these parameters would give rise to nonsingle exponential kinetics. First of all, different molecules may have different adsorption sites, giving rise to an inhomogeneous distribution of coupling matrix elements between the adsorbate and the adsorption site. This coupling is directly related to the forward-electron-transfer process. Second, the injected electrons may be trapped at sites that are at different distances away from the oxidized adsorbate and have different trap energies below the conduction band, giving rise to a distribution of coupling matrix elements and driving forces for the back-ET process. Although an inhomogeneous distribution of adsorbates at different adsorption sites can also contribute to the distribution in the electronic coupling for the back-ET process, it is not explicitly considered in our modeling because of the lack of detailed knowledge of the distribution. Instead, it is included indirectly in the distribution of trap site dependent coupling matrix elements.

To calculate the back-ET kinetics, we need to know the spatial and energetic distribution of the injected electrons in TiO₂. Although the existence of a large density of trap states in these TiO₂ nanocrystalline thin films and nanoparticles is a well-accepted notion,^{28,43–45} at present, the knowledge of their spatial and energetic distribution is incomplete. In this section, we assume two models for the distribution of trapped electrons in TiO₂ nanoparticles, and the back-ET kinetics are calculated on the basis of these models. The predicted back-ET kinetics are compared with the experimental results to provide some insight into the interfacial ET process in TiO₂ nanomaterials.

(a) Probability Distribution Function. Trapping of electrons in TiO₂ nanoparticles has been observed to occur on the 100 fs time scale.^{46–49} It is reasonable to assume that recombination of electrons occurs from trapped states. Because of the lack of detailed information, we will use the simplest model for the spatial distribution of injected electrons. Assuming that the probability, $p(r) dr$, of finding an electron trapped at a site at distance, r , away from the adsorbate is proportional to the surface area at that distance, the probability distribution function on a spherical surface can be shown to be²⁴

$$p(r) = C2 \frac{r}{d^2} \quad \text{for} \quad r \leq r_0$$

$$p(r) = 0 \quad \text{for} \quad r > r_0 \quad (1)$$

where $C = d^2/r_0^2$ is the normalization constant, r_0 is the maximum distance away from the adsorbate, and d is the diameter of the sphere, as shown in Scheme 1. $C = 1$ if we assume electrons can populate the whole surface, i.e., $r_0 = d$.

(b) *Trap State Dependent Electronic Coupling and Back-ET Rate.* If the coulombic interaction between the injected electrons and the oxidized adsorbate is negligible, the wave function of the trapped electron is determined by the interaction potential between the electron and the trap site. Assuming a coulombic potential, the trap state can be described by a hydrogenic model with the mobile electron orbit around the trap center.⁵⁰ The energy of the electron below the conduction band, i.e., the binding energy in the trap site, and the wave function of the trapped electron are the eigenenergy and eigenfunction of the ground or 1s state. The trap energy is determined by the electron effective mass, m_e^* , the dielectric constant, ϵ , of the material, and the charge of the trap center, Z :

$$E_{1s} = -E = -E_H \frac{Z^2 m_e^*}{\epsilon^2 m_e} \quad (2)$$

where $-E_H = -13.6$ eV is the eigenenergy of the 1s orbital of hydrogen atom and m_e is the electron rest mass. Since both the dielectric constant and effective mass are the same for different sites in the same material, in this model, trap states with different trap energy can be attributed to a different effective charge of the trap center. The wave function of the trapped electron is given by

$$\psi_{1s} = A_{1s} e^{-r/a^*} \quad (3)$$

$$a^* = \frac{\epsilon}{Z} \frac{m_e}{m_e^*} a_0 = \sqrt{\frac{E_H}{E}} \frac{m_e}{m_e^*} a_0$$

where a^* is the effective Bohr radius of the trapped electron and a_0 is the Bohr radius of the hydrogen atom. Within this model, electrons in a deep trap state have a smaller effective Bohr radius and hence a more localized wave function compared to those in shallower trap sites.

Assuming that the wave function for electrons in the adsorbate molecules are much more localized, the electronic coupling of the trapped electrons with the adsorbate is proportional to the amplitude of the wave function of the trapped electrons at the adsorbate site. This leads to a distance and trap energy dependent coupling matrix element:

$$V(r, E)^2 = V_0^2 \exp \left[-2 \frac{r}{a_0} \sqrt{\frac{E(t) m_e^*}{E_H m_e}} \right] \quad (4)$$

where V_0 is the coupling matrix element at $r = 0$, which is taken as the Ti^{4+} site at which the $Fe^{III}(CN)_6^{3-}$ molecule is adsorbed.

The driving force for back electron transfer from the conduction band edge to the adsorbate is denoted as ΔG_0 . For trapped electrons, the driving force for back ET becomes $\Delta G_0 + E$. Applying Marcus theory for nonadiabatic electron transfer⁵¹ to this case, one gets a distance and trap energy dependent back-electron-transfer rate:

$$k(r, t) = k(0) \exp \left[-2 \frac{r}{a_0} \sqrt{\frac{E(t) m_e^*}{E_H m_e}} - \frac{2E(t)(\Delta G_0 + \lambda) + E(t)^2}{4\lambda RT} \right] \quad (5)$$

$$k(0) = \frac{V(0)^2}{\hbar} \sqrt{\frac{\pi}{\lambda kT}} \exp \left[-\frac{(\Delta G_0 + \lambda)^2}{4\lambda RT} \right]$$

where $k(0)$ is the back-ET rate for electrons trapped at the Ti^{4+} site to which the adsorbate binds.

(c) *Back-ET Kinetics.* Solving the master equation for population decay and integrating over all the possible surface area (see Appendix), we get the ground-state bleaching recovery kinetics due to the back-ET process:

$$\Delta A(t) = -C' \int_0^{r_0} \frac{2r}{r_0^2} \exp \left[\int_0^t -k(0) \exp \left[-\frac{r}{a_0} \sqrt{\frac{E(t) m_e^*}{E_H m_e}} - \frac{2E(t)(\Delta G_0 + \lambda) + E(t)^2}{4\lambda RT} \right] dt \right] dr \quad (6)$$

It is clear from eq 6 that several factors affect the back-ET kinetics. These include the extent of the spatial distribution of the trapped electrons r_0 , and the relaxation kinetics between trap states, $E(t)$. These parameters will be used as fitting parameters. The other parameters are obtained from literature values:

(1) *Effective Mass m_e^* .* The effective mass of electrons in TiO_2 has not been unambiguously determined. Reported values range from $1m_e$ for bulk anatase crystals,⁵² about $10m_e$ for nanocrystalline anatase thin films,⁵³ to $30m_e$ – $100m_e$ for bulk rutile crystals.⁵⁴ Whether anatase TiO_2 nanoparticles in the nanometer size range show any quantum confinement effect is still unclear,^{55–57} although the most recent paper by Serpone et al.⁵⁶ reported that no quantum confinement effects were observed for particles with diameters as small as 2.1 nm. Assuming an exciton Bohr radius of smaller than 1 nm, a dielectric constant of $\epsilon = 9$,⁵³ and a hole effective mass of $0.8m_e$,⁵³ the lower limit of electron effective mass can be estimated to be $1.2m_e$. A reasonable value for m_e^* should be $> 1.2m_e$, although the exact value is not known. For this paper, we adopted the value of $m_e^* = 10m_e$ for nanocrystalline TiO_2 thin films from the most recent paper by Enright et al.⁵³ We also explored a range of effective mass in most of the calculations discussed below. We found that different values of m_e^* changed the calculated overall rate of the process but they did not affect the calculated relative trend of size dependence and the conclusion of the origin of the nonexponential recombination behavior.

(2) *$k(0)$.* $k(0)$ is defined as the back-ET rate constant at the minimum separation between the injected electron and the adsorbed $Fe^{III}(CN)_6^{3-}$ molecule. In principle, the coupling matrix element, the driving force, and reorganization energy can be determined experimentally from the spectrum of the charge-transfer complex, and using these parameters the value for $k(0)$ can be calculated according to eq 5. However, the inhomogeneous broadening of the charge-transfer band hinders an accurate determination of these parameters. Instead, we will use an approximate value of $k(0)$ directly measured by experiment. At the minimum separation the injected electron can be considered as localized on the Ti^{4+} site that formed a complex with the adsorbate. The electronic coupling for back ET from this site should be stronger than that for trap sites further away from the adsorbate. The corresponding back-ET rate from this site should also be faster. We hypothesize that the local electronic coupling may resemble that of a CN-bridged mixed valence dimer between Ti^{IV} and Fe^{II} . Fast back-ET times on the subpicosecond or faster time scale have been observed for many CN-bridged mixed valence molecular dimers.^{33,39,41,61} We also observed a similar fast back-ET component in the TiO_2 – $Fe(CN)_6^{4-}$ complex. As shown in Table 1, a 1–2 ps component was observed in all four samples. We attribute this fast component to back ET of electrons localized at the Ti^{4+} site that formed a complex with the adsorbate. Therefore, we assume $k(0) = 1/1.5 \text{ ps}^{-1}$ in our calculations. Of course, the overall

recombination kinetics are much more complicated, since the injected electron can also be trapped at Ti⁴⁺ sites further away from the adsorbate, giving rise to slower recombination components.

Attempts to directly measure the back-ET time in a CN-bridged Ti^{IV} and Fe^{II} mixed valence dimer have not been successful so far. Instead, we have investigated the [Ti^{IV}–Fe^{II}–(CN)₆]_n polymeric complex, which has a structure similar to the Fe^{II}–Fe^{III} Prussian Blue complex.⁶⁰ In [Ti^{IV}–Fe^{II}(CN)₆]_n, the Fe^{II} to Ti^{IV} charge-transfer band is located at about 400 nm.^{58,59} When excited at 400 nm, [Ti–Fe(CN)₆]_n in aqueous solution showed a bleach of the charge-transfer band centered at 400 nm.⁵⁹ The bleach recovery kinetics measured at 430 nm consist of a fast monoexponential bleaching recovery component (ca. 80%) with a time constant of about 1.4 ps and a long-lived component with lifetime of >100 ps. Spectral overlap of the bleach with the absorption of an intermediate species as well as contribution from vibrational cooling dynamics complicates the assignment of the back-ET time. A detailed analysis of the transient data for the [Ti–Fe(CN)₆]_n complex is ongoing.⁵⁹ In an earlier study of the Fe^{II}–Fe^{III} Prussian Blue complex, a similar fast bleach recovery component with a rate constant of ca. 300 fs was attributed to a fast back-ET process.⁶⁰ If we can attribute the fast bleach recovery component in the [Ti–Fe(CN)₆]_n complex to fast back ET, it would provide further support for our estimate of $k(0) = 1/1.5 \text{ ps}^{-1}$ used in the TiO₂–Fe^{II}(CN)₆⁴⁻ system.

(3) *Driving Force* (ΔG_0). The flat-band potential of nanocrystalline TiO₂ thin films in aqueous solution has been found to follow Nernstian's rule:^{62–64}

$$V_{fb} = -0.4 - 0.06 \cdot \text{pH (SCE)}$$

This value was found to be about 40 mV more negative than that for colloidal nanoparticles in aqueous solution.⁶⁵ The difference may be attributed to the involvement of surface states below the band edge in the colloidal system. Therefore, the value for nanocrystalline thin films instead of that for colloidal nanoparticles is a more accurate estimate of conduction band edge position. At pH = 2, the conduction band edge is estimated at –0.52 V (SCE). Desilvestro et al.⁶⁶ observed that TiO₂–Fe^{III}(CN)₆³⁻ complexes could be reduced by hydroquinone, indicating a lower limit of the redox potential at ca. +0.44 V. At pH = 2, the lower limit of the free energy difference for the back-ET reaction from the conducting band edge to the adsorbed Fe^{III}(CN)₆³⁻ can be estimated to be about –0.96 V. Because of the uncertainty in the redox potential, we have explored a range of driving forces from –0.94 to –1.4 V in our calculation. As will be discussed below, the qualitative conclusion regarding the nonexponential behavior and size dependence does not depend on the exact value of this parameter.

(4) *Reorganization Energy* (λ). Blackbourn et al.³⁸ reported a resonance Raman spectrum of the charge-transfer complex Fe^{II}(CN)₆⁴⁻/TiO₂ in aqueous solution. They identified 10 Raman active vibrational modes ranging from 2118 to 364 cm^{–1}. Using the simplest model of two displaced harmonic potential surfaces,^{33,35} the inner sphere reorganization energy can be calculated to be 0.315 eV (2550 cm^{–1}) on the basis of the spectrum. The value for outer-sphere reorganization is not well established for an interfacial ET process. Using a typical value of outer-sphere reorganization of ca. 0.3 V, a total reorganization energy of about 0.6 V is used for all the calculations presented below. By exploring a range of driving forces from –0.94 to –1.4 eV in the calculation, it should cover the effect of a small uncertainty in the reorganization energy.

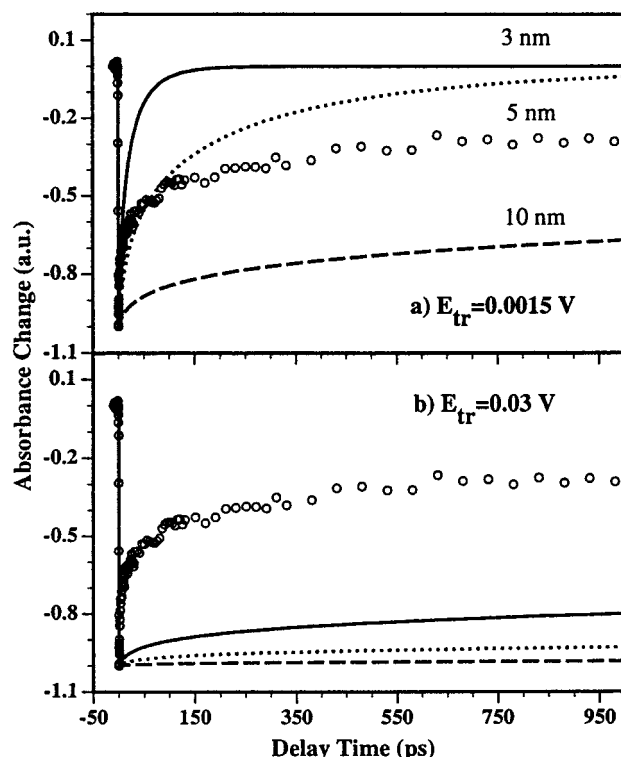


Figure 7. Calculated back-ET kinetics according to model 1 (eq 7) for particles with diameters of 3 nm (solid lines), 5 nm (dotted lines), and 10 nm (dashed lines) at a trap energy of (a) 0.0015 V and (b) 0.03 V. Also shown for comparison are observed kinetics for the 11 nm A-type particles (open circles). Fitting parameters are $k(0) = 1/1.5 \text{ ps}^{-1}$, $\Delta G_0 = -0.94 \text{ V}$, $\lambda = 0.60 \text{ V}$, $m_e^* = 10m_e$.

3. Model I: Random Spherical Distribution of Electrons.

In model I, we assume that (i) the injected electrons randomly populate the surface of the entire spherical particle, (ii) diffusion or electron hopping between trap states is negligible on the <1 ns time scale, and (iii) all trap states have the same energy.

Essentially, in this model, we assume a homogeneous distribution of energetically equivalent sites on the surface of the nanoparticles and the same probability of populating each site. Electron recombination from sites far away from the adsorbate will be slower compared to that from closer sites, giving rise to nonexponential recombination kinetics. Since we assume that there is only one trap state, the back-ET rate is no longer time dependent. Integrating over the entire spherical surface, eq 6 is simplified to

$$\Delta A(t) = -C' \int_0^d 2 \frac{r}{d^2} \exp \left[-k(0) \exp \left[-2 \frac{r}{a_0} \sqrt{\frac{Em_e^*}{E_H m_e}} - \frac{2E(\Delta G_0 + \lambda) + E^2}{4\lambda RT} \right] t \right] dr \quad (7)$$

where C' is a proportionality constant that relates the density of injected electrons to the amplitude of the observed bleach.

The main interest of this calculation is to show the dependence of the back-ET dynamics on the size of the particle. The parameters that affect the size dependence are the trap energy E and the effective mass m_e^* . The free energy change ΔG_0 and reorganization energy λ are chosen at –0.94 and +0.6 eV, respectively. The calculated back-ET kinetics based on eq 7 for particle sizes of 3, 5, and 10 nm are shown in Figure 7a for a trap energy of 0.0015 eV, and Figure 7b shows calculations for a trap energy of 0.03 eV. This model predicts a significant

size dependence in the back-ET kinetics. An effective mass of $10m_e$ for electrons was used in the calculation. A smaller effective mass leads to faster but still size dependent recombination rates. The experimentally observed size dependence is much smaller than that predicted by this model, suggesting that the injected electrons do not populate the surface of the entire particle on the < 1 ns time scale. Obviously, this model cannot fit the observed kinetics in $\text{Fe}^{\text{II}}(\text{CN})_6^{4-}/\text{TiO}_2$ system. However, the simplicity of the model offers some insight into the distance and trap energy dependence of the recombination rate. Electrons trapped at larger distances have smaller couplings with the adsorbate, leading to a smaller recombination rate. Within this random distribution model, larger particles will have more electrons trapped at longer distances, and hence a slower recombination rate as shown in Figure 7a,b. Electrons trapped at deeper trap states will have a more localized wave function and smaller coupling with the adsorbate. With the same particle size, electrons at a deeper trap will recombine slower, as clearly shown by the comparison of (a) and (b) of Figure 7.

Trapping of electrons has two effects on the back-ET rate. The driving force for electrons in deep trap states is smaller than shallow trap states. Since this reaction is believed to fall in the inverted region,^{25,26,29} trapping would decrease the activation barrier for the back ET and increase the rate. On the other hand, the wave function of electrons in deep trap states is more localized, so at the same distance its electronic overlap with the oxidized adsorbate molecule is smaller. This leads to a smaller coupling matrix element, and a slower recombination rate. The effect of the reduced coupling seems to dominate the overall rate change for our system. O'Regan et al.⁶⁷ investigated the back ET on a nanocrystalline TiO_2 thin film electrode sensitized by $\text{Ru}(\text{dcbpy})_3$. By biasing the Fermi level of the TiO_2 positive to the flat band potential by 300 mV, the back electron recombination rate could be sharply reduced by a factor of 10^3 . More recently, Haque and co-workers²⁸ observed similar bias dependent recombination kinetics in $\text{Ru}(\text{dcbpy})_2(\text{SCN})_2$ -sensitized nanocrystalline thin film electrodes. They found a decrease in the nonexponential back-ET rate when the films were biased slightly more positive than the conduction band edge. It was argued that when the Fermi level of TiO_2 became more positive than the flat band potential, deeper trap states were emptied. The photoinjected electron could then be trapped at these states, leading to a slower recombination reaction. These observations are consistent with our modeling result that back ET from deep trap states are slower than the shallow traps and a distribution of electrons in trap states leads to nonexponential kinetics.

Models assuming randomly distributed electrons have been used by other authors to describe electron recombination with adsorbate molecules or holes in semiconductor nanoparticles. Recently, Kelly and co-workers applied a two-dimensional random electron distribution model to account for the early time dynamics of the photoexcited electron and hole recombination in MoS_2 ,⁶⁸ and the back-ET kinetics from MoS_2 nanoparticle to the oxidized adsorbate molecules.⁶⁹ MoS_2 nanoparticles have a layered structure and a random distribution of electrons on the edge of the disk was used in the modeling. Both the kinetics of electron hole recombination and back electron transfer to the adsorbate were found to be well fit by the distributed kinetics predicted on the basis of a two-dimensional random distribution model. The applicability of the random distribution model depends on the delocalization extent of electrons in the conduction band of these nanoparticles. MoS_2 particles studied by Kelly and co-workers show a quantum confinement effect, indicating that the conduction band electrons can be delocalized

over the entire layer of the particle. A 2-D random distribution model would be appropriate for this system. Martini et al.²⁴ recently extended the 2-D random distribution model into a three-dimensional spherical surface. Their study of the back-ET time in the TiO_2 /anthracene system showed that there was no difference in the back-ET kinetics in 4 and 40 nm particles and the random distribution model did not fit their observed results.²⁴ The TiO_2 nanoparticles studied by Martini et al.²⁴ and in this paper, which have diameters > 2.1 nm, are not quantum confined.⁵⁶ The injected electrons in the conduction band are not delocalized over the entire particle, so rapid trapping^{46–49} would lead to a distribution that is not random over the entire spherical surface.

Although three assumptions are made in model I, the predicted size dependent kinetics are a direct consequence of assuming random distribution of injected electrons over the entire surface of the particles. This model always predicts slower kinetics in bigger particles, because of the distance dependent back-ET rate. Assumptions (ii) and (iii) do not change the size dependent nature of the model. In fact, Martini et al.²⁴ have shown that if diffusion between trap states is much faster than back ET, the back-ET kinetics become single exponential, which is not what we observed experimentally. More importantly, the model would still predict significant size dependent recombination kinetics, contradictory to the observed results. This model can be easily modified to accommodate multiple or a distribution of trap state energies.²⁴ Trap states with different energies will lead to different back-electron-transfer kinetics, but they are still size dependent.

4. Model II: Partially Localized Electrons with Distribution of Trap Energy. In model II, we assume the following. (i) Injected electrons randomly populate around a small region near the parent adsorbate. The size of the region is determined by fitting. (ii) Spatial diffusion or hopping between trap sites is negligible on the nanosecond time scale. (iii) Injected electrons relax from shallow to deep trap states.

On the basis of the results of model I, it is clear that the injected electrons do not randomly populate the surface of the entire particle on the < 1 ns time scale. In this model, we will assume that the injected electrons are distributed randomly on the surface up to a maximum distance r_0 away from the adsorbate. The exact value for r_0 , which is smaller than the diameter of the particles, will be determined by fitting. Another difference from model I is the consideration of the trapping dynamics, $E(t)$, of the injected electrons.

(a) Trapped Electron Relaxation Dynamics: $E(t)$. (1) Trap State Distribution. Assumption III deals with the relaxation of electrons between trap states. It is well-known that there is a large density of trap states in nanocrystalline TiO_2 particles and films,^{45,63} and trap state filling plays an important role in interfacial electron-transfer^{28,67} and carrier transport^{43,70} kinetics in nanocrystalline thin films. However, the exact distribution of trap state energy is not well established. Two types of measurements of trap state density distributions have been reported in the literature. The first class of experiments involved photoelectrochemical measurements of thin film electrodes.^{45,63} By measuring the optical absorption spectra of the nanocrystalline thin films under different external bias voltages, the distribution of trap states could be inferred. Rothenberger et al.⁶³ showed that both exponential and Gaussian distributions of trap state energetics could be used to account for the bias absorption spectra of the thin film. Another class of experiments used more direct techniques such as STM^{71,72} or electron energy loss measurements.⁷³ Measurements on single rutile crystal

surfaces showed a prominent peak of trap state at 0.37⁷¹ or 0.6 eV⁷³ below the conduction band. Measurements of polycrystalline native TiO₂ materials⁷² revealed a much higher density of surface states and a much broader distribution compared to single crystals. Since no direct measurement of colloidal nanoparticles in solution have been made, we assume that their trap state distribution function resembles that of the polycrystalline TiO₂ materials.^{63,72}

(2) *Experimental Determination of $E(t)$.* In our previous studies, we have observed that the infrared absorption signal of injected electrons in colloidal TiO₂ nanoparticles and thin films showed decay kinetics on the picosecond to nanosecond time scale.^{10,11,27} The decay rate was found to be faster in colloidal nanoparticles than in thin films and bulk single crystals, consistent with the trend of trap density in these materials. Although the detailed origin of the IR absorption of electrons is yet to be determined, a transition from a trap state to the conduction band is a very likely possibility. The absorption cross section depends on the density of the final states. For semiconductors, the density of states decreases as the kinetic energy of the electrons in the conduction band decreases.⁷⁴ Thus, as electrons move from shallow to deep trap states, the density of final states in the IR absorption of electrons decreases, leading to a decrease in the absorption cross section. If the distribution of the conduction band density of states is known, the IR cross section decay can be related to the decay of trap energy.

We have previously observed that at 2000 cm⁻¹, a frequency far away from the CN stretching band of the adsorbates, the mid-IR absorption signal in the Fe(CN)₆⁴⁻-TiO₂ nanoparticle (5 nm A type) complex is dominated by the absorption of electrons in TiO₂.²⁷ At this wavelength, the IR absorption of the injected electrons decays faster than the recombination kinetics, indicating that the absorption cross section of the electrons decays on the <1 ns time scale. If we assume a time dependent average cross section $\sigma(t)$ for the injected electrons, the time dependent mid-IR absorption signal, $A(t)$, can be described by

$$A(t) = N_e(t) \sigma(t) \quad (8)$$

where $N_e(t)$ is the density of injected electrons. Since the electron density is proportional to the amplitude of the CN bleach, the average cross section of electrons can be calculated by dividing the observed absorbance change at 2000 cm⁻¹ by the bleach recovery kinetics. The calculated average cross section according to this procedure can be described by a multiexponential decay function with time constants and amplitudes (in parentheses) of 7 ps (8%), 35 ps (22%), 300 ps (40%), and $\gg 1$ ns (30%).²⁷

For many semiconductor materials with a large defect density, the density of conduction band states decays roughly exponentially with energy near the conduction band edge.⁷⁴ It appears reasonable for us to assume an exponential function to describe the density of states in the conduction band of TiO₂ nanoparticles near the band edge,

$$\rho_c(E_c) = \alpha_c e^{\alpha_c E_c} \quad (9)$$

where α_c is the decay constant and E_c is the energy above the conduction band edge. From a recent band structure calculation of bulk rutile TiO₂,⁷⁵ we estimated that the density of states near the conduction band edge could be approximately described by an exponential decay with an α_c value of 12 eV⁻¹. We use the same value of α_c to describe the anatase thin film. The absorption cross section is proportional to the density of final

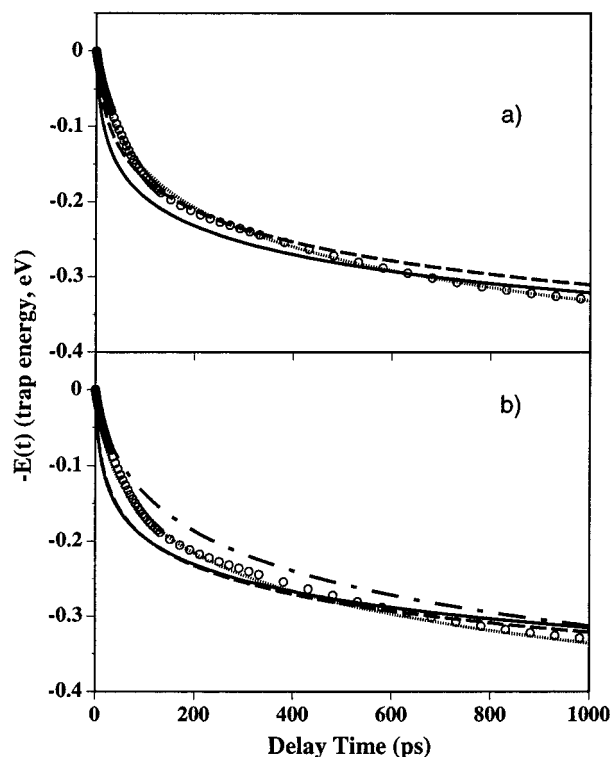


Figure 8. Comparison of electron relaxation kinetics, $E(t)$, calculated from the measured IR cross section decay for 5 nm A-type particles²⁷ according to eq 11 (open circles) and from fitting parameters of model II according to eq 14 (lines). (a) Comparison of $E(t)$ for 5 nm particles. The dotted line is the best fit to $E(t)$ calculated from the IR cross section decay with $\alpha = 12.5$ eV⁻¹ and $\beta = 0.00055$ eV²/ps. $E(t)$ calculated with parameters from the fits to the kinetics data for 5 nm nanoparticles are shown by the solid line for $\Delta G_0 = -0.94$ V, $\alpha = 19$ eV⁻¹, and $\beta = 0.0011$ eV²/ps and by the dashed line for $\Delta G_0 = -1.40$ V, $\alpha = 16$ eV⁻¹, and $\beta = 0.00069$ eV²/ps. (b) Comparison of $E(t)$ calculated from the fitting parameters listed in Table 2 with $\Delta G_0 = -0.94$ V for samples of 3 nm B-type particles (dot-dashed line), 9 nm B-type particles (dotted line), 5 nm A-type particles (dashed line), and 11 nm A-type particles (solid line).

states in the conduction band that is connected by the probe IR photon for a given trap energy, $E(t)$:

$$\sigma(t) = C \alpha_c e^{\alpha_c (E_{IR} - E(t))} \quad (10)$$

where E_{IR} is the energy of the IR probe photon and C is a proportionality constant. The normalized cross section at time t can be directly related to the trap energy

$$\frac{\sigma(t)}{\sigma(0)} = e^{-\alpha_c E(t)} \quad (11)$$

$$E(t) = -\frac{1}{\alpha_c} \ln \left(\frac{\sigma(t)}{\sigma(0)} \right)$$

Using the equation above and the experimentally determined cross section, we calculated the decay of the average trap energy. As shown in Figure 8a (open circles), the trap energy decays down to about 0.32 eV below the band-edge in 1 ns. This value appears to fall in the range of reported values for trap energy.^{71,73}

(3) *Models of Electron Relaxation.* Since we only have the experimentally determined cross section decay for the A-type 5 nm particles, we cannot use the experimentally determined $E(t)$ to fit the back-ET kinetics for all samples. Instead, we will assume a reasonable functional form of $E(t)$ and fit the back-ET kinetics to obtain the parameter for the $E(t)$ decay. A

TABLE 2: Fitting Parameters for Four Different Samples According to Model II

| samples | ΔG_0 , eV | α , eV ⁻¹ | β , eV ² /ps | r_0 , nm |
|--------------|-------------------|-----------------------------|-------------------------------|------------|
| A-type 5 nm | -0.94 | 18 | 0.001 0 | 0.80 |
| A-type 5 nm | -1.40 | 16 | 0.000 56 | 1.08 |
| A-type 11 nm | -0.94 | 19 | 0.001 1 | 0.80 |
| A-type 11 nm | -1.40 | 16 | 0.000 69 | 1.08 |
| B-type 3 nm | -0.94 | 12 | 0.000 29 | 1.00 |
| B-type 3 nm | -1.40 | 10 | 0.000 25 | 1.24 |
| B-type 9 nm | -0.94 | 13 | 0.000 46 | 0.86 |
| B-type 9 nm | -1.4 | 10 | 0.000 40 | 1.10 |

functional form of $E(t)$ can be derived if we assume a trap state distribution and relaxation mechanism. We will use an exponential decay function similar to that used by Rothenberger et al.⁶³ to model the density of trap states as a function of trap energy:

$$\rho(E) = \alpha e^{-\alpha E} \quad (12)$$

Here, $\rho(E)$ is a normalized density distribution function for the trap states and E , the trap energy, is defined relative to the conduction band edge. A larger positive E corresponds to a deep trap state.

The detailed mechanism of electron relaxation between trap states is not known. If we assume that the dominant relaxation occurs between trap states with small energy differences and the relaxation rate depends on the density of the trap states at lower energy, we can derive the rate equation for the trap energy decay:

$$\frac{dE}{dt} = kN_0\rho(E + dE) \approx kN_0\rho(E) \quad (13)$$

where N_0 is the total number of accessible trapped states.

Solving the equation above, an expression for the $E(t)$ can be obtained:

$$E(t) = \frac{\ln(\alpha^2\beta t + 1)}{\alpha} \quad (14)$$

where $\beta = kN_0$ is a product of a relaxation rate constant and the total number of the accessible trap sites.

As shown in eq 6, the back-ET kinetics depend on the trap energy decay kinetics $E(t)$. As will be shown later, an observed kinetics trace will lead to a unique fit for $E(t)$. This fitting procedure does not depend on the exact model to describe the trap state distribution and trap energy relaxation, as long as it provides a functional form that can describe $E(t)$. Nevertheless it is interesting to note that the trap energy decay obtained from experiment can be well described by eq 14 derived from the simple model outlined above. The best fit of the data, shown by the dotted line in Figure 8a, yields a value of $\alpha = 12.5$ eV⁻¹ and $\beta = 0.000 55$ eV²/ps.

(b) *Fitting of the Back-ET Kinetics.* Using eqs 6 and 14, we fitted all the recombination kinetics with r_0 , α , and β as fitting parameters. Listed in Table 2 are the fitting parameters for the four different particle sizes with $\lambda = 0.6$ eV, $m_e^* = 10m_e$, and two values for $\Delta G_0 = -0.94$ and -1.4 V. For a given ΔG_0 , λ , and m_e^* , a unique combination of the three fitting parameters, r_0 , α , and β , that can produce a satisfactory fit to the data, is obtained. Examples of two such fits are shown in Figure 6 for the 3 nm B-type and 5 nm A-type particles assuming $\Delta G_0 = -0.94$. Equally good fits can be obtained for $\Delta G_0 = -1.4$ V. For each pair of α and β values, a trap energy relaxation function, $E(t)$, for trapped electrons is determined according to eq 14. Shown in Figure 8a is a comparison of the relaxation

kinetics for 5 nm A-type particles calculated from the experimentally determined IR cross section decay according to eq 11 (open circles) and the fitted $E(t)$ with $\Delta G_0 = -0.94$ V (solid line) and -1.4 V (broken line), respectively. Although the trap energy relaxation kinetics obtained from the fits are not in perfect agreement with the observed electron relaxation kinetics, they have the overall shape of the relaxation and qualitatively similar trap energy. Considering the simplicity of the models used to describe the trap state distribution and relaxation, the agreement is rather satisfactory. Similar relaxation kinetics obtained from fitting the four samples with $\Delta G_0 = -0.94$ V are shown in Figure 8b. Different electron relaxation kinetics are needed to fit the noticeable difference in the recombination kinetics of A- and B-type particles. Within this model, these differences in the back-ET kinetics can be attributed the difference in trap state distribution and relaxation in these materials, presumably caused by the different chemistry used in the preparation process.

For the four samples of different particle sizes, we obtained a maximum distance of the injected electrons from the adsorbate of about 0.8–1.24 nm. This result suggests that the injected electrons are localized near the adsorbate instead of randomized over the entire particle surface. These values are much smaller than the diameter of the particles, which explains the observed lack of size dependence in back-ET kinetics. The rather localized electron distribution is also consistent with the observed pump power independence of the recombination kinetics. The localized electron distribution may be a result of the large effective mass of electrons in TiO₂. Assuming $m_e^* = 10m_e$, $\epsilon = 9$, and an effective mass of $0.8m_e$ for holes, the exciton Bohr radius in TiO₂ can be estimated to be about 0.6 nm. As can be seen in eq 6, the value of r_0 obtained from the fitting scales inversely with the square root of effective mass. A smaller effective mass will lead to a larger value of r_0 . At the lower limit of electron effective mass of $1.2m_e$, the values for r_0 would be about 2.3–3.6 nm, which are still smaller than most of the particle sizes studied.

Summary

We have studied the back-ET kinetics in Fe^{II}(CN)₆⁴⁻-sensitized TiO₂ nanoparticle colloid in aqueous solution. The main experimental results follow.

(1) The observed non-single-exponential back-ET kinetics were found to be independent of the pump power under our experimental conditions, indicating a geminate recombination process.

(2) Comparison of the back-ET kinetics between samples of 5 and 11 nm A-type particles or between samples of 3 and 9 nm B-type particles shows very little differences. These results suggest that in the size range studied, the back-ET kinetics are independent of the particle size.

(3) There is a noticeable difference in the back-ET kinetics for samples of A- and B-type nanoparticles, indicating the important role of surface chemistry in the back-ET process.

To provide detailed insight into the back-ET process, we calculated the back-ET kinetics in two model distributions of trapped electrons. Model I, which assumed a random distribution of electrons on the entire surface of the particle, predicted a large size dependence in the ET kinetics and therefore could not fit the observed kinetics. Model II, which assumed a localized distribution of injected electrons and relaxation of electrons from shallow to deep trap states, was found to produce a satisfactory fit to the back-ET data with three fitting

parameters. The electron relaxation kinetics $E(t)$ obtained from the fit were in reasonable agreement with that obtained from the experimentally determined IR cross section decay. These fitting parameters should only be considered as approximate values because of the simple models used in describing conduction band density of state distribution, trap state distribution and relaxation mechanism. Nevertheless, we consider the main findings of the model to be qualitatively correct and the insight about the back-ET process to be valuable. According to the fitting results of model II, the injected electrons were localized near the adsorbate, leading to size independent recombination kinetics. The small difference in the back-ET kinetics between the samples of A- and B-type particles could be accounted for by the difference in the electron relaxation kinetics caused by different surface chemistry. The non-single-exponential kinetics are a result of back ET from trap states at a different distance from the adsorbate and with different trap energies. Electrons in deep trap states and at longer distances recombine more slowly with the adsorbate due to a smaller electronic coupling matrix element.

Acknowledgment. The work is supported in part by Petroleum Research Fund, administered by the American Chemical Society, and the National Science Foundation CAREER award under grant No. 9733796. We would also like to thank Prof. Fred Menger and Mr. Jason Kieper in the chemistry department of Emory University for their help in the particle size measurements.

Appendix: Derivation of Eq 6

The density of electrons trapped at a distance r away from the adsorbate can be described by

$$\frac{dN_e(r,t)}{dt} = -k(r,t) N_e(r,t)$$

Rearranging the equation and integrating from $t = 0$ to t , we obtain

$$\ln \frac{N_e(r,t)}{N_e(r,0)} = \int_0^t -k(r,t) dt$$

The measured absorbance change at the charge-transfer band is proportional to the density of excited molecules, $\Delta N_T(t)$, which equals the total density of injected electrons:

$$\begin{aligned} \Delta A(t) &= -\epsilon l \Delta N_T(t) = -\epsilon l \int_0^{r_0} N_e(r,t) dr \\ &= -\epsilon l \int_0^{r_0} N_e(r,0) \exp\left[-\int_0^t k(r,t) dt\right] dr \end{aligned}$$

where ϵ is the extinction coefficient of the CT complex at the probing wavelength and l is the path length of the sample. At $t = 0$, the density of injected electrons at any given distance r is determined by the distribution function and total density of injected electrons:

$$N_e(r,0) = N_0 P(r)$$

Inserting the expression for $P(r)$, eq 1, and $k(r,t)$, eq 5, into the equation above, we get

$$\Delta A(t) = -\epsilon l N_0 \int_0^{r_0} \frac{2r}{r_0^2} \exp\left[\int_0^t -k(0) \exp\left[-\frac{2r}{a_0} \sqrt{\frac{E(t)m_e^*}{E_H m_e}} - \frac{2E(t)(\Delta G_0 + \lambda) + E(t)^2}{4\lambda RT}\right] dt\right] dr$$

where $\epsilon l N_0$ is treated as a scaling factor and, for simplicity, was set to be 1.

References and Notes

- (1) Miller, R. J. D.; McLendon, G. L.; Nozik, A. J.; Schmickler, W.; Willig, F. *Surface electron-transfer processes*; VCH publishers, Inc.: Deerfield Beach, FL, 1995.
- (2) Nozik, A. J.; Memming, R. J. *Phys. Chem.* **1996**, *100*, 13061.
- (3) Kamat, P. V. *Prog. React. Kinet.* **1994**, *19*, 277–316.
- (4) Jacobson, K. I.; Jacobson, R. E. *Imaging Systems*; John Wiley & Sons: New York, 1976.
- (5) Kay, A.; Gratzel, M. *Solar Energy Mater. Solar Cells* **1996**, *44*, 99–117.
- (6) Serpone, N. *Res. Chemical Intermed.* **1994**, *20*, 953–992.
- (7) Colvin, V. L.; Schlamp, M. C.; Alivisatos, A. P. *Nature* **1994**, *370*, 354–357.
- (8) Oregan, B.; Gratzel, M. *Nature* **1991**, *353*, 737–740.
- (9) Asbury, J. B.; Ellingson, R. J.; Ghosh, H. N.; Ferrere, S.; Nozik, A. J.; Lian, T. J. *Phys. Chem. B* **1999**, *103*, 3110–3119.
- (10) Ghosh, H. N.; Asbury, J. B.; Lian, T. J. *Phys. Chem. B* **1998**, *102*, 6482–6486.
- (11) Asbury, J. B.; Ghosh, H. N.; Ellingson, R. J.; Ferrere, S.; Nozik, A. J.; Lian, T. Femtosecond IR Study of Ru Dye Sensitized Nanocrystalline TiO₂ Thin Films: Ultrafast Electron Injection and Relaxation Dynamics. *Ultrafast Phenomena XI*, 1998.
- (12) Ellingson, R. J.; Asbury, J. B.; Ferrere, S.; Ghosh, H. N.; Lian, T.; Nozik, A. J. *J. Phys. Chem. B* **1998**, *102*, 6455.
- (13) Cherepy, N. J.; Smestad, G. P.; Gratzel, M.; Zhang, J. Z. *J. Phys. Chem.* **1997**, *101*, 9342.
- (14) Martini, I.; Hodak, J. H.; Hartland, G. V.; Kamat, P. V. *J. Chem. Phys.* **1997**, *107*, 8064.
- (15) Martini, I.; Hodak, J. H.; Hartland, G. V. *J. Phys. Chem. B* **1998**, *102*, 9508.
- (16) Heimer, T.; Heilweil, E. J. *J. Phys. Chem. B* **1997**, *101*, 10990–10993.
- (17) Heimer, T.; Heilweil, E. J. Measuring Ultrafast Sensitizer-TiO₂ Electron Dynamics with Mid-Infrared Spectroscopy. *Ultrafast Phenomena XI*, 1998.
- (18) Tachibana, Y.; Moser, J. E.; Gratzel, M.; Klug, D. R.; Durrant, J. R. *J. Phys. Chem.* **1996**, *100*, 20056–20062.
- (19) Hannappel, T.; Burfeindt, B.; Storck, W.; Willig, F. *J. Phys. Chem. B* **1997**, *101*, 6799.
- (20) Burfeindt, B.; Hannappel, T.; Storck, W.; Willig, F. *J. Phys. Chem.* **1996**, *100*, 16463.
- (21) Rehm, J. M.; McLendon, G. L.; Nagasawa, Y.; Yoshihara, K.; Moser, J.; Gratzel, M. *J. Phys. Chem.* **1996**, *100*, 9577–9578.
- (22) Murakoshi, K.; Yanagida, S.; Capel, M.; Castner, J. E. W. *Interfacial Electron-Transfer Dynamics of Photosensitized Zinc Oxide Nanoclusters*; ACS Symposium Series 679; American Chemical Society: Washington, DC, 1997.
- (23) Murakoshi, K.; Yanagida, S.; Castner, J. E. W. Personal communication.
- (24) Martini, I.; Hodak, J. H.; Hartland, G. J. *Phys. Chem. B* **1999**, *103*, 9104.
- (25) Martini, I.; Hodak, J. H.; Hartland, G. V. *J. Phys. Chem. B* **1998**, *102*, 607–614.
- (26) Moser, J. E.; Gratzel, M. *Chem. Phys.* **1993**, *176*, 493.
- (27) Ghosh, H. N.; Asbury, J. B.; Weng, Y.; Lian, T. J. *Phys. Chem. B* **1998**, *102*, 10208.
- (28) Haque, S. A.; Tachibana, Y.; Klug, D. R.; Durrant, J. R. *J. Phys. Chem. B* **1998**, *102*.
- (29) Lu, H.; Prieskorn, J. N.; Hupp, J. T. *J. Am. Chem. Soc.* **1993**, *115*, 4927–4928.
- (30) Vrachnou, E.; Vlachopoulos, N.; Graetzel, M. *J. Chem. Soc., Chem. Commun.* **1987**, 868.
- (31) Liu, D.; Fessenden, R. W.; Hug, G. L.; Kamat, P. V. *J. Phys. Chem. B* **1997**, *101*, 2583.
- (32) Hush, N. S. *Electrochim. Acta* **1968**, *13*, 1005.
- (33) Tominaga, K.; Klinner, D. A. V.; Johnson, A. E.; Levinger, N. E.; Barbara, P. F. *J. Chem. Phys.* **1993**, *98*, 1228–1243.
- (34) Hupp, J. T.; Dong, Y. H.; Blackburn, R. L.; Lu, H. J. *Phys. Chem.* **1993**, *97*, 3278.
- (35) Myers, A. B. *Chem. Phys.* **1994**, *180*, 215–230.

- (36) Klaas, W.; Hochstrasser, R. M. Coherence and Adiabaticity in Ultrafast Electron Transfer. In *Electron Transfer: From Isolated Molecules to Biomolecules. Part II*; Jortner, J., Bixon, M., Eds.; Advances in Chemical Physics; Wiley: New York, 1999; Vol. 107; p 263.
- (37) Bahnemann, D.; Henglein, A.; Lilie, J.; Spanhel, L. *J. Phys. Chem.* **1984**, 88, 709.
- (38) Blackburn, R.; L.; Johnson, C. S.; Hupp, J. T. *J. Am. Chem. Soc.* **1991**, 113, 1060.
- (39) Doorn, S. K.; Dyer, R. B.; Stoutland, P. O.; Woodruff, W. H. *J. Am. Chem. Soc.* **1993**, 115, 6398–6405.
- (40) Spears, K. G.; Wen, X. N.; Zhang, R. H. *J. Phys. Chem.* **1996**, 100, 10206–10209.
- (41) Wang, C.; Akhremitchev, B.; Walker, G. C. *Laser Chem.* **1999**, 19, 385.
- (42) Kamat, P. V.; Bedja, I.; Hotchandani, S.; Patterson, L. K. *J. Phys. Chem.* **1996**, 100, 4900–4908.
- (43) Schwarzburg, K.; Willig, F. *Appl. Phys. Lett.* **1991**, 58, 2520–2522.
- (44) Kay, A.; Humphrybaker, R.; Gratzel, M. *J. Phys. Chem.* **1994**, 98, 952–959.
- (45) Boschloo, G.; Fitzmaurice, D. *J. Phys. Chem. B* **1999**, 103, 2228–2231.
- (46) Colombo, D. P., Jr.; Bowman, R. M. *J. Phys. Chem.* **1996**, 100, 18445.
- (47) Colombo, D. P.; Bowman, R. M. *J. Phys. Chem.* **1995**, 99, 11752–11756.
- (48) Skinner, D. E.; Colombo, D. P.; Cavaleri, J. J.; Bowman, R. M. *J. Phys. Chem.* **1995**, 99, 7853–7856.
- (49) Serpone, N.; Lawless, D.; Khairutdinov, R.; Pelizzetti, E. *J. Phys. Chem.* **1995**, 99, 16655–16661.
- (50) Brus, L. *J. Phys. Chem.* **1986**, 90, 2555–2560.
- (51) Marcus, R. A.; Sutin, N. *Biochim. Biophys. Acta* **1985**, 811, 265.
- (52) Tang, H.; Prasad, K.; Sanjines, R.; Schmid, P. E.; Levy, F. *J. Appl. Phys.* **1994**, 75, 2042.
- (53) Enright, B.; Fitzmaurice, D. *J. Phys. Chem.* **1996**, 100, 1027–1035.
- (54) Breckenridge, R. G.; Hosler, W. R. *Phys. Rev.* **1953**, 91, 793.
- (55) Kavan, L.; Stoto, T.; Gratzel, M.; Fitzmaurice, D.; Shklover, V. *J. Phys. Chem.* **1993**, 97, 9493–9498.
- (56) Serpone, N.; Lawless, D.; Khairutdinov, R. *J. Phys. Chem.* **1995**, 99, 16646–16654.
- (57) Kormann, C.; Bahnemann, D. W.; Hoffmann, M. R. *J. Phys. Chem.* **1988**, 92, 5196.
- (58) Ayers, J. A.; Waggoner, W. H. *J. Inorg. Nucl. Chem.* **1971**, 33, 721–733.
- (59) Weng, Y.; Wang, Y.; Asbury, J. B.; Ghosh, H.; Lian, T. Manuscripts in preparation.
- (60) Arnett, D. C.; Vohringer, P.; Scherer, N. F. *J. Am. Chem. Soc.* **1995**, 117, 12262–12272.
- (61) Reid, P. J.; Silva, C.; Barbara, P. F.; Karki, L.; Hupp, J. T. *J. Phys. Chem.* **1995**, 99, 2609–2616.
- (62) Hagfeldt, A.; Gratzel, M. *Chem. Rev.* **1995**, 95, 49–68.
- (63) Rothenberger, G.; Fitzmaurice, D.; Gratzel, M. *J. Phys. Chem.* **1992**, 96, 5983–5986.
- (64) Redmond, G.; Fitzmaurice, D. *J. Phys. Chem.* **1993**, 97, 1426–1430.
- (65) Duonghong, D.; Ramsden, J.; Gratzel, M. *J. Am. Chem. Soc.* **1982**, 104, 2977.
- (66) Desilvestro, J.; Pons, S.; Vrachnou, E.; Gratzel, M. *J. Electroanal. Chem.* **1988**, 246, 411.
- (67) O'Regan, B.; Moser, J.; Anderson, M.; Gratzel, M. *J. Phys. Chem.* **1990**, 94, 8720–8726.
- (68) Doolen, R.; Laitinen, R.; Parsapour, F.; Kelley, D. F. *J. Phys. Chem. B* **1998**, 102, 3906.
- (69) Butoi, C. I.; Langdon, B. T.; Kelley, D. F. *J. Phys. Chem. B* **1998**, 102, 9635–9639.
- (70) Konerkamp, R.; Henninger, R.; Hoyer, P. *J. Phys. Chem.* **1993**, 97, 7328.
- (71) Fan, F.-R. F.; Bard, A. J. *J. Phys. Chem.* **1990**, 94, 3761.
- (72) Casillas, N.; Snyder, S.; Smyrl, W.; White, H. *J. Phys. Chem.* **1991**, 95, 7002–7007.
- (73) Chung, Y. W.; Lo, W. J.; Somorjai, G. A. *Surf. Sci.* **1977**, 64, 588.
- (74) Pankove, J. I. *Optical Processes in Semiconductors*; Dover: New York, 1975.
- (75) Sorantin, P. I.; Scharz, K. *Inorg. Chem.* **1992**, 31, 567–576.